ELECTRICAL AND MAGNETIC PROPERTIES OF MULTIFERROIC $Co_{0.6}Zn_{0.4}Fe_{1.7}Mn_{0.3}O_4$ DOPED $0.99Bi_{0.47}Na_{0.47}Ba_{0.06}TiO_3$-$0.01Ba(Sn_{0.70}Nb_{0.24})O_3$ CERAMICS SYNTHESIZED VIA THE SOLID-STATE COMBUSTION TECHNIQUE

Anupong Luangpangai[1], Phomphon Chuai[1], Aurawan Rittidech[2], Supree Pinitsoontorn[3], Pongsakorn Jantaratana[4], Naratip Vittayakorn[5], Thanya Udeye[1,6,*], and Theerachai Bongkarn[1,6]

Received: August 24, 2024; Revised: February 01, 2025; Accepted: February 01, 2025

Abstract

Multiferroic (1-x)[$0.99Bi_{0.47}Na_{0.47}Ba_{0.06}TiO_3$-$0.01Ba(Sn_{0.70}Nb_{0.24})O_3$]-x$Co_{0.6}Zn_{0.4}Fe_{1.7}Mn_{0.3}O_4$ (abbreviated as BNBT-BSN-xCZFMO) ceramics with x ranging from 0 to 0.20 were fabricated using the solid-state combustion technique. The effect of varying BNBT-BSN : CZFMO ratios on the phase structure, microstructure, electrical and magnetic properties was investigated. X-ray diffraction (XRD) analysis of pure BNBT-BSN showed a perovskite structure with rhombohedral and tetragonal phases. The doped BNBT-BSN-xCZFMO ceramics displayed coexisting rhombohedral, tetragonal, and cubic spinel phases, with the cubic spinel phase increasing when the CZFMO content increased. In addition, the XRD peaks shifted to higher angles as the CZFMO content increased, indicating a decrease in lattice parameters. The dielectric constant decreased with higher CZFMO content and higher frequencies. The pure BNBT-BSN ceramic exhibited a saturated P-E loop with a P_{max} of 33.2 μC/cm^2, P_r of 26.1 μC/cm^2, and an E_c of 14.5 kV/cm. With increased CZFMO content, non-saturated and bloated P-E loops with lower P_{max}, P_r, and E_c were observed, implying a rise in the leakage current. The addition of CZFMO induced ferromagnetic behavior in the ceramics, leading to an increase in M_s and a reduction in H_c as CZFMO content increased. The magnetoelectric coupling coefficient of BNBT-BSN-xCZFMO ceramics continuously increased with higher CZFMO content.

Keywords: **BNBT-BSN-xCZFMO; Dielectric; Ferroelectric; Ferromagnetic; Phase Structure**

---

[1] *Department of Physics, Faculty of Science, Naresuan University, Phitsanulok, 65000, Thailand. E-mail: anupongl66@nu.ac.th; phomphonc64@nu.ac.th; thanyau@nu.ac.th*[*]*; researchcmu@yahoo.com*

[2] *Department of Physics, Faculty of Science, Mahasarakham University, Mahasarakham 44150, Thailand. E-mail: aurawan.r@msu.ac.th*

[3] *Institute of Nanomaterials Research and Innovation for Energy (IN-RIE), Khon Kaen University, Khon Kaen 40002, Thailand. E-mail: psupree@kku.ac.th*

[4] *Department of Physics, Faculty of Science, Kasetsart University, Bangkok 10900, Thailand. E-mail: fscipsj@ku.ac.th*

[5] *Advanced Materials Research Unit, Faculty of Science, King Mongkut's Institute of Technology Ladkrabang, Bangkok 10520, Thailand. E-mail: naratip.vi@kmitl.ac.th*

[6] *Research Center for Academic Excellence in Applied Physics, Faculty of Science, Naresuan University, Phitsanulok, 65000, Thailand.*

[*] *Corresponding author*

DOI: https://doi.org/10.55766/sujst10883

Suranaree J. Sci. Technol. 32(4):030326(1-14)

Introduction

Due to their excellent electrical and piezoelectric properties, the electronic device industry commonly uses lead-based ceramics, such as lead zirconate titanate (PZT). However, the lead vapors produced during synthesis are hazardous to human health and the environment. Consequently, there is a need to replace lead-based ceramics with lead-free alternatives like bismuth sodium titanate ($Bi_{0.5}Na_{0.5}TiO_3$), potassium sodium niobate ($K_{0.5}Na_{0.5}NbO_3$), and barium titanate ($BaTiO_3$) (Li *et al*., 2013; Parija *et al*., 2013; Lee *et al*., 2015). Bismuth sodium titanate ($Bi_{0.5}Na_{0.5}TiO_3$; BNT) lead-free ceramics are particularly attractive due to their superior electrical properties, including a high Curie temperature (T_C=540°C) and remnant polarization (P_r=38 μC/cm^2). However, a large coercive field (E_C=73 kV/cm) limits practical application, resulting in a low piezoelectric coefficient (d_{33}) (Nagata *et al*., 2006). To fix these limitations, solid solutions such as barium titanate ($BaTiO_3$), barium calcium titanate ($Ba_{0.7}Ca_{0.3}TiO_3$), bismuth potassium titanate ($Bi_{0.5}K_{0.5}TiO_3$), and strontium titanate ($SrTiO_3$) have been added to BNT ceramics (Zou *et al*., 2010; Chandrasekhar and Kumar, 2015; Cao *et al*., 2016; Wang and Shi, 2023). Introducing 6% $BaTiO_3$ into the BNT system produced $Bi_{0.47}Na_{0.47}Ba_{0.06}TiO_3$ (BNBT) ceramics at a morphotropic phase boundary (MPB) condition. This composition, recently fabricated by B. Thatawong *et al*. (Thatawong *et al*., 2022) using the solid-state combustion technique, showed a high maximum dielectric constant (ε_m=8405), remnant polarization (P_r=28.2 μC/cm^2), and piezoelectric coefficient (d_{33}=161 pC/N). The structure's complexity allows for modification using various conditions like electric field and temperature, which can enhance the ceramic's electrical properties (Li *et al*., 2016).

The BNBT system at the MPB requires modifications to optimize its properties further. This generally involves adding a solid solution with a similar structure to create a trinary system in BNBT, enhancing specific properties like dielectric and ferroelectric performance (Swain *et al*., 2015). Y. Jia *et al*. (Jia *et al*., 2015) incorporated $Ba(Sn_{0.70}Nb_{0.24})O_3$ (BSN) into BNBT using the traditional solid-state method, resulting in high strain properties (S_{max} of 0.43%, d_{33}* of 633 pm/V), a good maximum dielectric constant (ε_m) of approximately 4000 and a large maximum polarization (P_{max}) of around 40 μC/cm^2. Recently, A. Luangpangai *et al*. (Luangpangai *et al*., 2024) successfully fabricated $0.99Bi_{0.47}Na_{0.47}Ba_{0.06}TiO_3$-$0.01BaSn_{0.70}Nb_{0.24}O_3$ (BNBT-BSN) ceramics using the solid-state combustion technique. The ceramics were calcined at 800°C for 2 hours and sintered at 1175°C for 2 hours. This ceramic exhibited an MPB between rhombohedral and tetragonal phases with an excellent ε_m of 6513, a large P_r of 28.98 μC/cm^2, and a high P_{max} of 42.21 μC/cm^2.

Ferromagnetic materials with a spinel ferrite structure (AB_2O_4) have been widely employed in various devices, with potential future applications in multiferroic systems (Xiao *et al*., 2010). Among these, a $Co_{0.6}Zn_{0.4}Fe_{1.7}Mn_{0.3}O_4$ (CZFMO) ceramic was successfully synthesized by P. Thawong *et al*. (Thawong *et al*., 2019) using the solid-state combustion technique with a low firing temperature and short dwell time (calcined at 750°C for 2 hours and sintered at 1200°C for 2 hours). The ceramic showed a good dielectric constant (ε) of 365 and high ferromagnetic properties (M_s of 72.50 emu/g and H_c of 4.24 Oe).

Multiferroic materials are typically made by combining two or more ferroelectric, ferromagnetic, or ferroelastic phases. The goal of the combination is to take advantage of the specific properties of each phase and improve the overall multiferroic behavior. Many reports have documented progress in developing lead-free multiferroic materials that feature a perovskite structure with ferroelectric and spinel ferrite ferromagnetic phases. For example, CZFMO-modified $Ba_{0.85}Ca_{0.15}Ti_{0.9}Zr_{0.1}O_3$ systems exhibited improved ferromagnetic properties (M_s of 6.32 emu/g and M_r of 0.55 emu/g) and a magnetoelectric coupling coefficient (α_E) of -2.415 mV/Oe·cm, as reported by M. Singh *et al*. (Singh *et al*., 2020). Similarly, E. Venkata Ramana *et al*. (Venkata Ramana *et al*., 2012) prepared BNBT ceramics doped with CZFMO using the conventional solid-state reaction technique. This ceramic demonstrated a good P_r of 12.5 μC/cm^2, an M_s of 13.6 emu/g, and an α_E of 7.8 mV/Oe.cm. This suggests that adding CZFMO, with its spinel structure, into lead-free ceramics is a promising approach for improving ferroelectric, ferromagnetic, and magnetoelectric properties. As a result, the potential of improving these properties in BNBT-BSN with CZFMO is interesting. Notably, the investigation of multiferroic BNBT-BSN-CZFMO ceramics remains largely unexplored.

In this study, multiferroic (1-x)$[0.99Bi_{0.47}Na_{0.47}Ba_{0.06}TiO_3$-$0.01Ba(Sn_{0.70}Nb_{0.24})O_3]$-x$Co_{0.6}Zn_{0.4}Fe_{1.7}Mn_{0.3}O_4$ (BNBT-BSN-xCZFMO) ceramics with x between 0 and 0.20 were synthesized using the solid-state combustion technique and their phase structure, microstructure, electrical, magnetic and magnetoelectric properties were investigated.

Materials and Methods

The solid-state combustion technique was used to fabricate multiferroic (1-x)[0.99$Bi_{0.47}Na_{0.47}Ba_{0.06}TiO_3-0.01Ba(Sn_{0.70}Nb_{0.24})O_3$]-x$Co_{0.6}Zn_{0.4}Fe_{1.7}Mn_{0.3}O_4$ (BNBT-BSN-xCZFMO) ceramics with x ranging from 0 to 0.20. The BNBT-BSN and CZFMO components were prepared separately using the stoichiometric ratio. $Bi(NO_3)_3.5H_2O$ (98.50%, KEMAUS, AU), $NaNO_3$ (99.00%, Ajex Finechem, AU), $Ba(NO_3)_2$ (99.00%, HiMedia, USA), TiO_2 (99.00%, KEMAUS, AU), SnO_2 (99.00%, Sigma-Aldrich, USA) and Nb_2O_5 (99.00%, Eleps, RUS) were the raw materials for BNBT-BSN. While, CZFMO raw materials consisted of $Co(NO_3)_2.6(H_2O)$ (98.00%, Ajex Finechem, AU), ZnO (99.00%, Merck German, DE), $Fe(NO_3)_3.9H_2O$ (101.00%, Ajex Finechem, AU) and MnO_2 (99.00%, Sigma-Aldrich, USA). The raw materials were ball milled using zirconium balls in an ethanol solution for 24 hours. After drying, the slurries were ground and combined with glycine ($C_2H_5NO_2$: 99.00%, KemAus, AUS) as fuel at a propellant ratio of 1.1111 wt% for BNBT-BSN and 0.855 wt% for CZFMO. The BNBT-BSN and CZFMO powders were calcined separately at 850°C for 2 hours and 750°C for 2 hours, respectively, with a 5°C/min heating rate. The calcined BNBT-BSN and CZFMO powders were combined at the desired weight ratio (x = 0 to 0.20), mixed with polyvinyl butyral (PVB), and pressed into green pellets with a diameter of 15 mm and a thickness of 1 mm under 80 MPa of pressure. Finally, the green pellets were sintered at 1175°C for 2 hours, with a heating rate of 2°C/min.

The phase structure of the ceramics was characterized by X-ray diffraction (XRD, Bruker, D8 Discover) with Cu-Kα1,2 radiation, scanning in the 2θ range of 10° to 70° at room temperature. Phase analysis was conducted using the Rietveld refinement method via the Fullprof program. The microstructure of the sample surfaces was examined with scanning electron microscopy (SEM, Thermo Fisher Scientific, Apreo S), after thermally etching 100°C below the sintering temperature. The average grain size was determined using the linear intercept method, based on measurements of over 300 grains. Sample density was calculated using Archimedes method.

To measure the electrical and magnetoelectric properties, silver paste (IRMS sp5574, CN) was coated on both sides of the samples and fired at 550°C for 20 min to make electrodes. Temperature and frequency-dependent dielectric properties were measured using LCR meters (Agilent 4284A and HP4284A, respectively). The polarization versus electric field (P-E) hysteresis loops were measured with a computer-controlled modified Sawyer-Tower circuit (Radiant, PLC2-The P-E loop). Ferromagnetic hysteresis (M-H) loops were obtained using a vibrating sample magnetometer (Versa Lab, Quantum Design). Magnetoelectric coupling was analyzed with a lock-in amplifier (Stanford Research System, model SR830).

Results and Discussion

X-ray diffraction (XRD) was used to determine the phase structure of BNBT-BSN-xCZFMO ceramics. Figure 1(a) displays the XRD patterns of the BNBT-BSN-xCZFMO samples with CZFMO content between 0 and 0.20, in the 2θ range of 10 to 70°. The pure BNBT-BSN ceramic showed a pure perovskite structure without any secondary phases. As the CZFMO content increased, the coexistence of perovskite and spinel phases was observed. Moreover, secondary phases of Bi_2O_3 (JCPDS files No. 29-0236) and Fe_2O_3 (JCPDS files No. 33-0664) were found for samples with x = 0.10, 0.15 and 0.20.

To further analyze the phase structure, Figure 1(b) focuses on the XRD in the 2θ range of 38° to 50°. This region includes indexed peaks for both perovskite and spinel phases. According to JCPDS data No. 36-0339 (Sinkruason *et al*., 2023), the tetragonal phase is identified by a single $(111)_T$ peak at 2θ of 40° and dual $(002)_T/(200)_T$ peaks at 2θ of 46°. While the rhombohedral phase is characterized by dual $(003)_R/(021)_R$ peaks at 2θ of 40° and a single $(202)_R$ peak at 2θ of 46°, according to JCPDS files No. 36-0340 (Sinkruason *et al*. 2023). Also, the cubic spinel phase is indexed by single $(400)_C$ and $(331)_C$ peaks at 2θ = 43° and 47°, respectively, according to JCPDS files No. 22-1086 (Jiang and Ai, 2010).

Pure BNBT-BSN ceramics showed split peaks at 2θ of 40° and 46°, indicating the coexistence of tetragonal and rhombohedral phases, consistent with observations by A. Luangpangai *et al*. (Luangpangai *et al*., 2024). When CZFMO content increased, these split peaks merged into asymmetric peaks. A small distinct single peak emerged at higher amounts of CZFMO (x = 0.15 and 0.20), suggesting the coexistence of perovskite and spinel phases. In addition, XRD peaks at 2θ of 40° and 46° moved slightly to a lower angle, implying an expansion in lattice parameters. This shift may be attributed to the substitution of Ti (0.605 Å) and Nb (0.640 Å) ions with larger Fe (0.645 Å) and Mn (0.645 Å) ions at the B-sites, leading to an extended lattice structure.

To quantify the phase structure content in BNBT-BSN-xCZFMO ceramics, the Rietveld refinement method was applied using the Fullprof program, as seen in Figure 2(a-e). Data sources for determining the lattice parameters, including length (a, b, c), angle (α, β, γ), atomic data, and occupancy rate, were obtained from the Crystallography Open Database (COD). To fit the XRD results of BNBT-BSN-xCZFMO ceramics, a combination of structures including tetragonal (P4bm space group), rhombohedral (R3c space group) and cubic spinel phase (Fd3m space group) was applied. A pseudo-

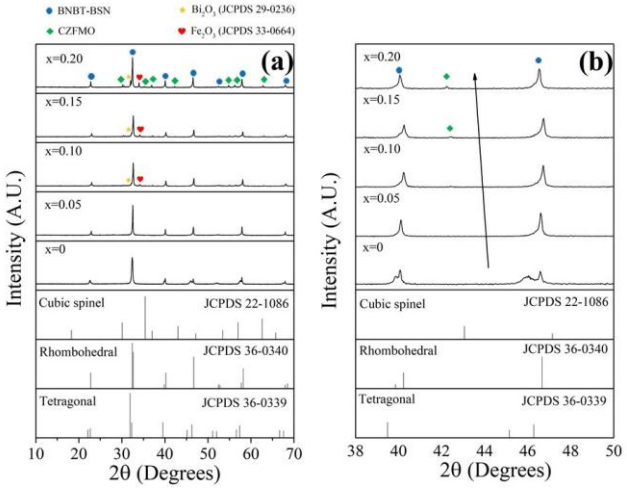

Figure 1. XRD patterns of BNBT-BSN-xCZFMO ceramics with different x, showing phase evolution with increasing CZFMO content, highlighting perovskite and spinel phases, at the 2θ range of (a) 10-70° and (b) 38-50°

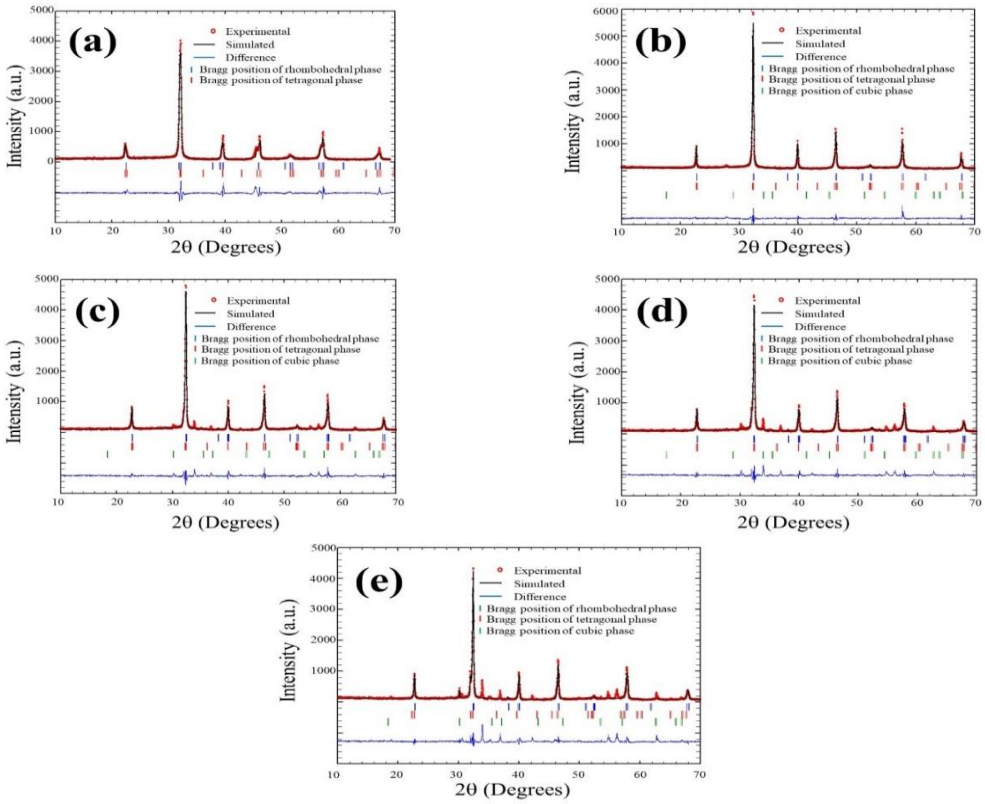

Figure 2. Rietveld refinement results for BNBT-BSN-xCZFMO ceramics with (a) x=0, (b) x=0.05, (c) x=0.10, (d) x=0.15, and (e) x=0.20

Voigt function was used to model the XRD peaks, while a Chebyshev polynomial fit the background. The fitting results, including lattice parameters and phase percentages, are presented in Table 1. The undoped BNBT-BSN ceramic showed a coexistence of tetragonal (T) and rhombohedral (R) phases with a nearly equal T-to-R phase ratio of 55:45, consistent with previous reports (Luangpangai *et al*., 2024). However, a cubic spinel (C) phase emerged alongside the R and T phases when CZFMO content increased. The proportion of the C phase continuously increased from 2% (x=0.05) to 7% (x=0.10), 14% (x=0.15), and 35% (x=0.20), as shown in Table 1. The increase in the C phase corresponds with the rising CZFMO content.

Table 1. The fitting parameters, lattices parameters, and phase percentages of BNBT-BSN-xCZFMO ceramics with x=0-0.20

Samples	Refine parameters	Phase structures	Profile parameters	Atoms information					The percentage of phase
				Label	*x*	*y*	*z*	Occ.	
x=0	χ^2=3.02 R_p=28.3% R_{wp}=26.1% R_{exp}=15.0%	*R3c:H*	*a*=5.5667Å *c*=13.8347Å *u*=0.2620 *v*=0.3810 *w*=0.0085	Na	0	0	0.2627	0.37280	45
				Bi	0	0	0.2627	0.38668	
				Ba	0	0	0.2627	0.06650	
				Ti	0	0	0.0063	0.66690	
				Sn	0	0	0.0063	0.04982	
				Nb	0	0	0.0063	0.01996	
				O	0.1260	0.3360	0.0833	3.23624	
		P4bm	*a*=5.5607Å *c*=3.9799Å *u*=0.4873 *v*=-0.3131 *w*=0.0889	Na	0	0.5	0.5450	0.41677	55
				Bi	0	0.5	0.5450	0.53575	
				Ba	0	0.5	0.5450	0.07168	
				Ti	0	0	0	0.93094	
				Sn	0	0	0	0.01012	
				Nb	0	0	0	0.15076	
				O1	0	0	0.5100	2.48962	
				O2	0.2710	0.2290	0.0150	0.84673	
x=0.05	χ^2=1.56 R_p=23.7% R_{wp}=20.6% R_{exp}=16.52%	*R3c:H*	*a*=5.5278Å *c*=13.5604Å *u*=-0.1211 *v*=0.1501 *w*=-0.0211	Na	0	0	0.2627	0.22182	35
				Bi	0	0	0.2627	0.38644	
				Ba	0	0	0.2627	0.03474	
				Ti	0	0	0.0063	0.61860	
				Sn	0	0	0.0063	0.03766	
				Nb	0	0	0.0063	0.01921	
				O	0.1260	0.3360	0.0833	3.39273	
		P4bm	*a*=5.5512Å *c*=3.9011Å *u*=1.4977 *v*=-0.1387 *w*=0.0012	Na	0	0.5	0.5450	0.55868	63
				Bi	0	0.5	0.5450	0.53618	
				Ba	0	0.5	0.5450	0.07593	
				Ti	0	0	0	0.94505	
				Sn	0	0	0	0.01222	
				Nb	0	0	0	0.15113	
				O1	0	0	0.5100	0.90793	
				O2	0.2710	0.2290	0.0150	1.76005	
		Fd-3 m	*a*=b=c=8.7308Å *u*=2.7826 *v*=2.6580 *w*=0.2997	O1	0.25000	0.25000	0.25000	1.41573	2
				Fe1	0.12500	0.12500	0.12500	0.28913	
				Fe2	0.50000	0.50000	0.50000	0.25732	
				Mn1	0.12500	0.12500	0.12500	0.04996	
				Mn2	0.50000	0.50000	0.50000	0.09905	
				Zn1	0.12500	0.12500	0.12500	0.18479	
				Zn2	0.50000	0.50000	0.50000	0.37077	
				Co1	0.12500	0.12500	0.12500	0.19708	
				Co2	0.50000	0.50000	0.50000	0.15199	
x=0.10	χ^2=2.21 R_p=25.8% R_{wp}=24.4% R_{exp}=16.45%	*R3c:H*	*a*=5.5183Å *c*=13.5696Å *u*=-0.1390 *v*=0.1842 *w*=-0.0193	Na	0	0	0.2627	0.69141	33
				Bi	0	0	0.2627	0.53550	
				Ba	0	0	0.2627	0.07603	
				Ti	0	0	0.0063	0.93320	
				Sn	0	0	0.0063	0.01244	
				Nb	0	0	0.0063	0.15101	
				O	0.1260	0.3360	0.0833	1.10965	
		P4bm	*a*=5.5474Å *c*=3.8945Å *u*=0.2809 *v*=0.3281 *w*=0.1429	Na	0	0.5	0.5450	0.69141	60
				Bi	0	0.5	0.5450	0.53550	
				Ba	0	0.5	0.5450	0.07603	
				Ti	0	0	0	0.93320	
				Sn	0	0	0	0.01244	
				Nb	0	0	0	0.15101	
				O1	0	0	0.5100	1.10965	
				O2	0.2710	0.2290	0.0150	2.13461	
		Fd-3 m	*a*=b=c=8.3805Å *u*=-4.8083 *v*=1.0261 *w*=2.6383	O1	0.25000	0.2290	0.25000	0.96274	7
				Fe1	0.12500	0.25000	0.12500	0.25924	
				Fe2	0.50000	0.12500	0.50000	0.44891	
				Mn1	0.12500	0.50000	0.12500	0.06639	
				Mn2	0.50000	0.12500	0.50000	0.16551	
				Zn1	0.12500	0.50000	0.12500	0.20346	
				Zn2	0.50000	0.12500	0.50000	0.41741	
				Co1	0.12500	0.50000	0.12500	0.21227	
				Co2	0.50000	0.12500	0.50000	0.20206	

Table 1. The fitting parameters, lattices parameters, and phase percentages of BNBT-BSN-xCZFMO ceramics with x=0-0.20

Samples	Refine parameters	Phase structures	Profile parameters	Atoms information					The percentage of phase
				Label	*x*	*y*	*z*	Occ.	
x=0.05	χ^2=3.03 R_p=28.9% R_{wp}=29.1% R_{exp}=16.72%	*R3c:H*	*a*=5.5189Å *c*=13.5778Å *u*=-0.1396 *v*=0.1955 *w*=-0.0211	Na	0	0	0	0.25054	32
				Bi	0	0	0	0.38575	
				Ba	0	0	0	0.03497	
				Ti	0	0	0	0.53010	
				Sn	0	0	0	0.03956	
				Nb	0	0	0	0.01905	
				O	0.1260	0.3360	0.3360	3.23577	
		P4bm	*a*=5.5463Å *c*=3.9015Å *u*=-0.2404 *v*=0.6001 *w*=0.1616	Na	0	0	0.5450	0.5450	54
				Bi	0	0	0.5450	0.5450	
				Ba	0	0	0.5450	0.5450	
				Ti	0	0	0	0	
				Sn	0	0	0	0	
				Nb	0	0	0	0	
				O1	0	0	0.5100	0.5100	
				O2	0.2710	0.2710	0.0150	0.0150	
		Fd-3 m	*a*=*b*=*c*=8.7684Å *u*=7.2525 *v*=8.1273 *w*=-0.4732	O1	0.25000	0.25000	0.25000	0.34779	14
				Fe1	0.12500	0.12500	0.12500	0.33121	
				Fe2	0.50000	0.50000	0.50000	0.16784	
				Mn1	0.12500	0.12500	0.12500	0.27678	
				Mn2	0.50000	0.50000	0.50000	0.07761	
				Zn1	0.12500	0.12500	0.12500	0.20674	
				Zn2	0.50000	0.50000	0.50000	0.36016	
				Co1	0.12500	0.12500	0.12500	0.17308	
				Co2	0.50000	0.50000	0.50000	0.15212	
x=0.20	χ^2=4.40 R_p=32.6% R_{wp}=34.7% R_{exp}=16.53%	*R3c:H*	*a*=5.5139Å c=13.5570Å *u*=-0.1077 *v*=0.1759 *w*=-0.0271	Na	0	0	0.2627	0.34239	45
				Bi	0	0	0.2627	0.38720	
				Ba	0	0	0.2627	0.03474	
				Ti	0	0	0.0063	0.60880	
				Sn	0	0	0.0063	0.03943	
				Nb	0	0	0.0063	0.01945	
				O	0.1260	0.3360	0.0833	5.56031	
		P4bm	*a*=5.5407Å *c*=3.9926Å *u*=1.0289 *v*=-0.2569 *w*=0.0314	Na	0	0.5	0.5450	0.16208	20
				Bi	0	0.5	0.5450	0.70116	
				Ba	0	0.5	0.5450	0.07574	
				Ti	0	0	0	0.96739	
				Sn	0	0	0	0.01247	
				Nb	0	0	0	0.15058	
				O1	0	0	0.5100	0.37308	
				O2	0.2710	0.2290	0.0150	6.21947	
		Fd-3 m	*a*=b=c=8.3920Å *u*=83.4376 *v*=4.3107 *w*=-7.2226	O1	0.25000	0.25000	0.25000	1.38011	35
				Fe1	0.12500	0.12500	0.12500	0.08221	
				Fe2	0.50000	0.50000	0.50000	0.30418	
				Mn1	0.12500	0.12500	0.12500	0.12982	
				Mn2	0.50000	0.50000	0.50000	0.17748	
				Zn1	0.12500	0.12500	0.12500	0.32256	
				Zn2	0.50000	0.50000	0.50000	0.42124	
				Co1	0.12500	0.12500	0.12500	0.53911	
				Co2	0.50000	0.50000	0.50000	0.53198	

A scanning electron microscope (SEM) was used to examine the microstructure of BNBT-BSN-xCZFMO ceramics with various CZFMO content. The surface morphology of these ceramics is illustrated in Figure 3(a)-(e). The undoped BNBT-BSN ceramic (x=0) had polygonal grain shapes with anisotropic grain growth (Figure 3(a)). When CZFMO content increased up to x=0.05, three different grain types emerged: rough-surface, smooth-surface, and rod-like grains, as seen in Figure 3(b). As x increased to 0.10 and 0.15, the rough-surface and rod-like grains diminished, while smooth-surface grains increased and merged, as shown in Figures 3(c) and (d). At higher CZFMO content (x=0.20), the smooth-surfaced grains were primarily distributed at the grain boundaries of rough-surface grains, and rod-like grains were not observed, as seen in Figure 3(e). Additionally, increased CZFMO content increased porosity at the grain boundaries, likely caused by excessive oxygen vacancies (Bongkarn *et al*., 2016).

Table 2 shows that the pure BNBT-BSN ceramic had an average grain size of 1.58 μm. When CZFMO content increased to 0.05, the average grain size significantly increased to 13.59 μm. This increase could be attributed to forming a liquid phase during the sintering process and creating oxygen vacancies, which enhanced mass transfer when CZFMO content increased (Zhang *et al*., 2017). However, the average grain size continuously decreased with further increases in CZFMO contents (x>0.05). This suggests that higher amounts of CZFMO accumulated at the grain boundaries, inhibiting grain growth (Kornphom *et al*., 2023).

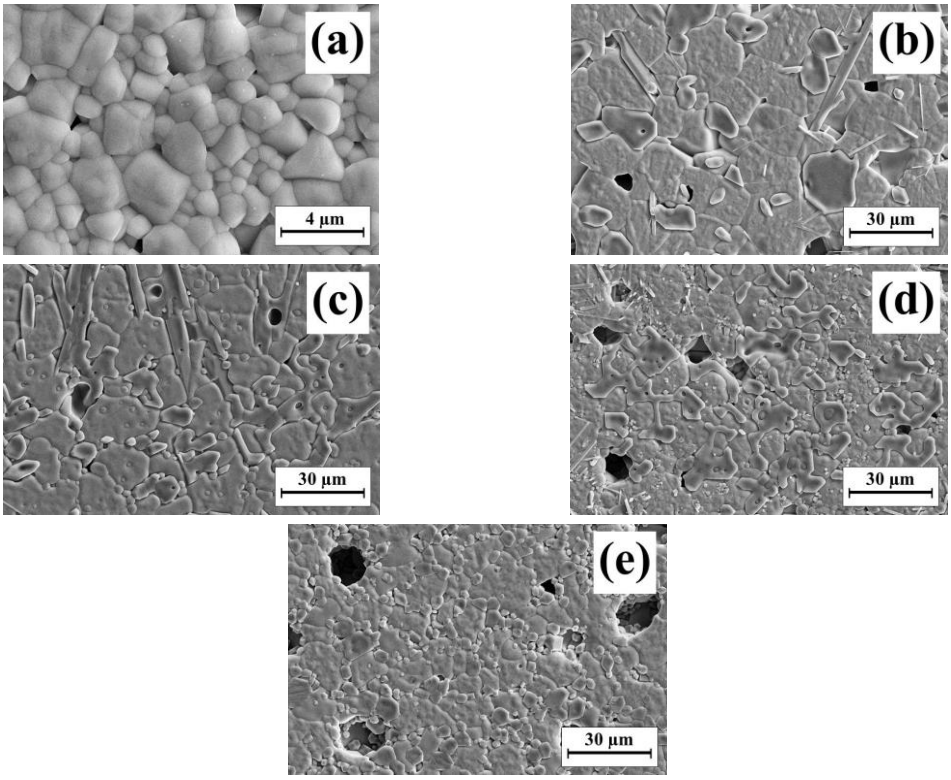

Figure 3. **Surface morphology of BNBT-BSN-xCZFMO ceramics with (a) x=0, (b) x=0.05, (c) x=0.10, (d) x=0.15, and (e) x=0.20**

Table 2. **The average grain size, density, dielectric, ferroelectric, and ferromagnetic properties of BNBT-BSN-xCZFMO ceramics with various x levels**

CZFMO contents	Average grain size (µm)	Density (g/cm^3)	ε_r at 1 kHz	$\tan\delta_r$ at 1 kHz	P_{max} ($\mu C/cm^2$)	P_r ($\mu C/cm^2$)	E_c (kV/cm)	M_s (emu/g)	M_r (emu/g)	H_c (Oe)	α_E (mV/Oe.cm)
x=0	1.58	5.54	1505	0.05	33.19	26.09	14.22	-0.0044	9×10^{-5}	52	1.317
x=0.05	13.59	5.32	952	0.02	14.68	5.16	11.06	0.0715	9×10^{-4}	24	2.743
x=0.10	12.39	5.21	674	0.03	11.30	11.73	24.99	0.1411	9×10^{-5}	7	3.655
x=0.15	6.70	5.10	501	0.03	5.45	3.01	17.40	0.2485	7×10^{-5}	3	4.402
x=0.20	4.52	5.05	364	0.03	3.80	2.09	17.39	0.8056	-	5	5.111

To investigate each specific grain type in the SEM images, energy dispersive spectroscopy (EDS) was used to identify and quantify the elemental composition of the grains, as shown in Figure 4. In the BNBT-BSN-0.05CZFMO ceramic, the rough-surface, smooth-surface, and rod-like grains were marked and labeled with Spectrum 1, Spectrum 2, and Spectrum 3, respectively. The rough-surface grain had a high concentration of Bi (48.5 wt%) and Ti (21.7 wt%). However, the smooth-surface grain had elevated levels of Co (3.1 wt%), Mn (1.4 wt%) and Fe (7.4 wt%), indicating the presence of ferroelectric and ferrite phases in the respective grains. Additionally, the rod-like grains contained a balance of Bi (13.2 wt%), Ba (13.7 wt%), Ti (32.9 wt%), Co (2.5 wt%), Mn (1.1 wt%) and Fe (4.8 wt%), indicating a coexistence of ferroelectric and ferrite structures, with more ferrite structures.

The EDS mapping confirmed the distribution of elements in the surface morphology of the BNBT-BSN-0.05CZFMO ceramic, as shown in Figure 5. It showed that Bi and Na were predominantly in ferroelectric grains, while only Ba, Ti, Co, and Fe are clearly seen in the ferrite and rod-like grains. This distribution supports the classification of different grain types within the material.

The density of the BNBT-BSN-xCZFMO ceramics gradually decreased from 5.54 to 5.05 g/cm^3 as the CZFMO content increased from 0 to 0.20, as listed in Table 2. This result corresponds with the SEM images, which revealed increased porosity and poor microstructure at higher CZFMO content.

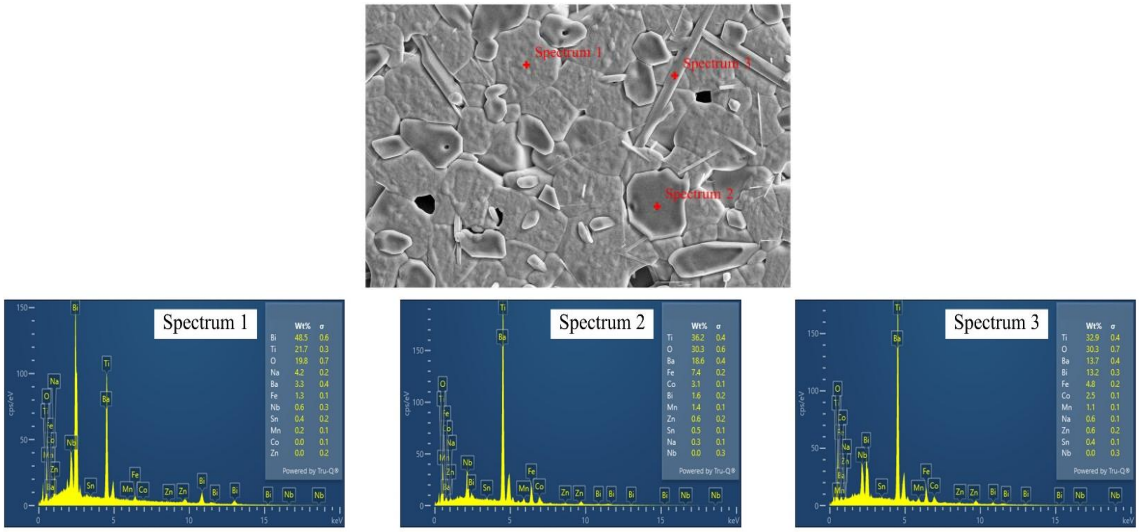

Figure 4. **EDS element analysis of the rough surface (spectrum 1), smooth surface (spectrum 2), and rod-like grains (spectrum 3) in the 0.95BNBT-BSN-0.05CZFMO ceramic**

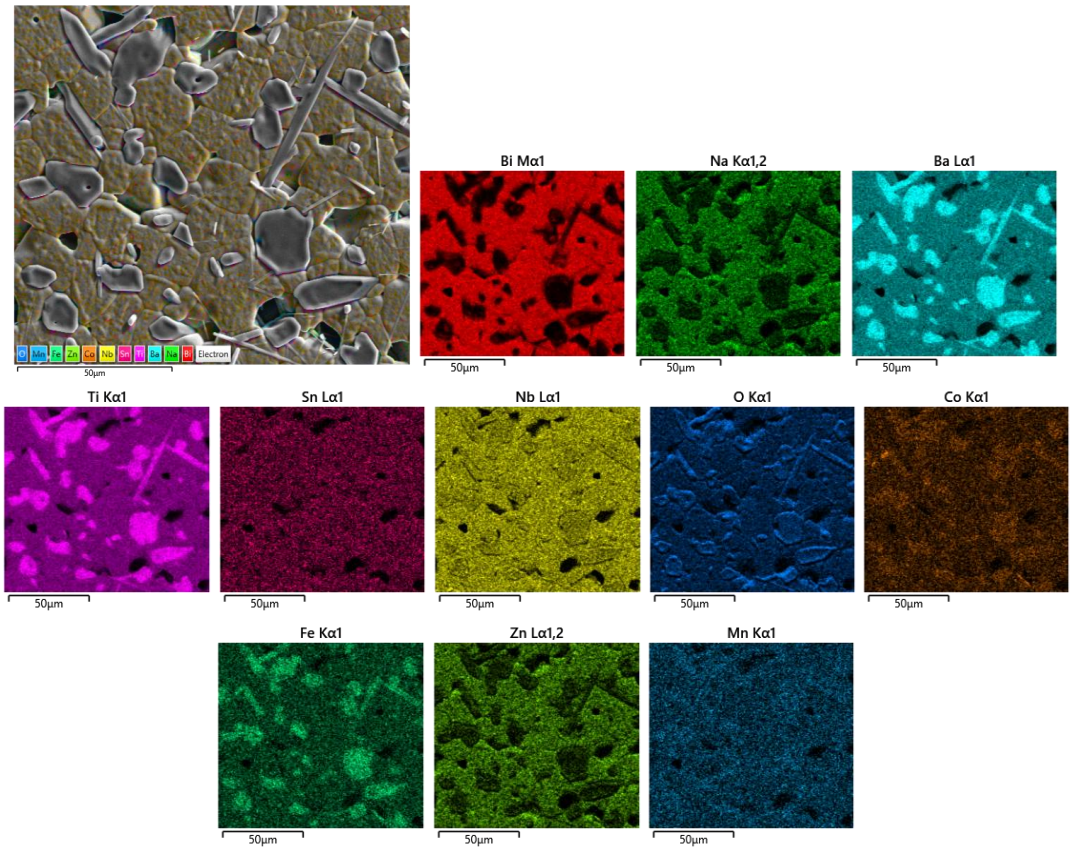

Figure 5. **EDS mapping analysis showing the elemental distribution in the surface morphology of the 0.95BNBT-BSN-0.05CZFMO ceramic**

The temperature-dependent dielectric constant (ε) and loss (tanδ) of BNBT-BSN-xCZFMO ceramics with varying CZFMO content are displayed in Figure 6(a-j). The measurements were taken from room temperature to 400°C at frequencies of 1, 10, and 100 kHz. In general, the dielectric curve of BNT-based ceramics shows two dielectric peaks. The first dielectric peak appears at the depolarization temperature (T_d), which marks the thermal transition of polar nanoregions (PNRs) from a rhombohedral structure (R3c symmetry) to a tetragonal structure (P4bm symmetry) (Badapanda *et al*., 2017). While the second dielectric peak is at T_m, the temperature where the dielectric constant reaches its maximum (Badapanda *et al*., 2017).

In Figure 6(a), the dielectric curve of the pure BNBT-BSN sample exhibited two dielectric peaks with T_d at 147°C and T_m at 278°C, measured at 1 kHz. The dielectric response is broad with frequency dispersion, characteristic of relaxor ferroelectric behavior, where T_d shifts to higher temperatures and T_m shifts to lower temperatures with increased frequency, as shown in Figure 6(a) (Luangpangai *et al*., 2024).

When a small amount of CZFMO (x=0.05) is added, the dielectric response and loss measured at 1 kHz significantly increased at high temperatures, and T_m disappears, as seen in Figure 6(c-d). As x increased to 0.10 (Figure 6(e)), the dielectric constant measured at 1 and 10 kHz rapidly increased with temperature, and T_d and T_m were not visible. Furthermore, at higher CZFMO content (x>0.10), the dielectric curve and loss dramatically increased with temperature, and T_d and T_m were not present at any frequency, as observed in Figure 6(g-j). These observations could be related to space charge polarization and higher ionic conductivity at higher temperatures resulting from CZFMO substitution inducing leakage currents (Nanda *et al*., 2019).

At 1 kHz, the dielectric constant (ε_r) gradually decreased from 1505 to 364, while dielectric loss ($\tan\delta_r$) slightly decreased from 0.05 to between 0.02 and 0.03 as CZFMO content increased from 0 to 0.20, as listed in Table 2. A decrease in ε may be due to multiple factors, including poor morphology, decreased density, and increased conductivity with the addition of CZFMO. The dielectric constant (ε_m) and loss ($\tan\delta_m$) at T_m, measured at 1 kHz, were 6536 and 0.03, respectively, in the pure BNBT-BSN sample. However, the ε_m and $\tan\delta_m$ values could not be calculated as the peaks were no longer present after adding CZFMO content, implying an increase in electrical conductivity (Wu *et al*., 2012).

Figure 7(a) and (b) illustrate the frequency-dependent ε and tanδ of BNBT-BSN-xCZFMO ceramics with varying CZFMO levels, measured from 10^2 to 10^5 Hz at room temperature. In all samples, ε decreased when the frequency increased, as shown in Figure 7(a). This aligns with the common understanding that the dielectric constant is highest at low frequencies because of multiple polarization mechanisms, such as electronic, space

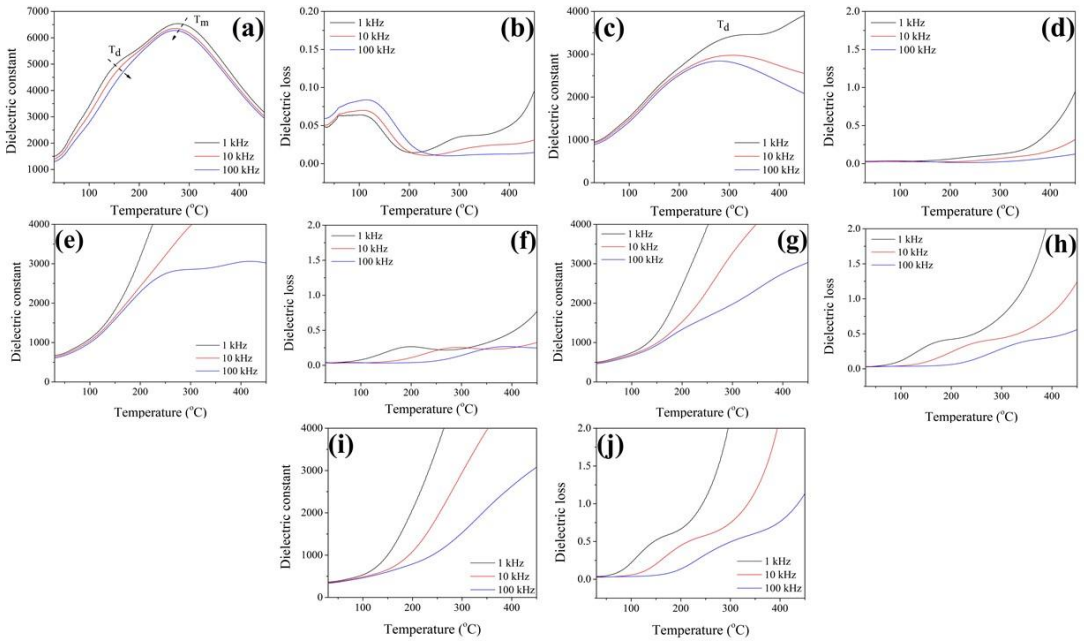

Figure 6. Temperature-dependent dielectric constant (ε) and loss tangent (tanδ) of BNBT-BSN-xCZFMO ceramics at (a), (b) x = 0, (c), (d) x = 0.05, (e), (f) x = 0.10, (g), (h) x = 0.15 and (i), (j) x = 0.20, measured from room temperature to 500°C at frequencies of 1, 10 and 100 kHz

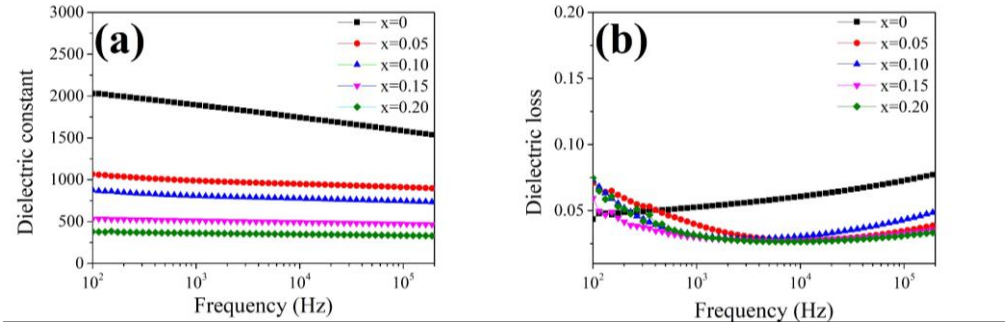

Figure 7. Frequency-dependent (a) ε and (b) tanδ of BNBT-BSN-xCZFMO ceramics with various x levels, over a frequency range of 10^2 to 10^5 Hz.

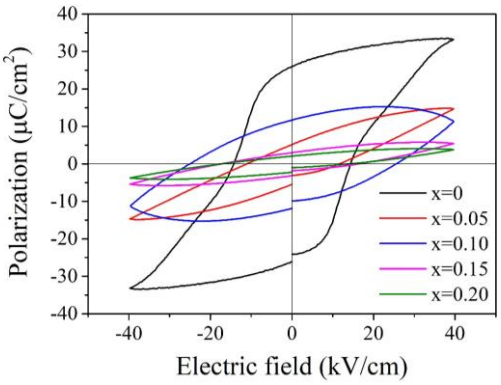

Figure 8. P-E hysteresis loops of BNBT-BSN-xCZFMO ceramics with varying x levels, under an electric field of 40 kV/cm.

charge, interfacial, ionic, and orientation polarization. As frequency increases, the dielectric constant gradually decreases until stabilizing at higher frequencies due to a reduced ability of the dipoles to align with the external electric field, causing a reduction in the orientation polarization (Zawar *et al*., 2019). Additionally, the tanδ at a low frequency of 10^2 Hz was similar between samples, ranging between 0.04 and 0.07, suggesting minimal impact from CZFMO content at these lower frequencies. However, as frequency increased, tanδ tended to decrease for all CZFMO-substituted samples, as represented in Figure 7(b). This result could be explained by dipole relaxation, caused by the electric dipoles' inability to change direction at higher frequencies of the applied electric field (Singh *et al*., 2011).

The polarization-electric field (P-E) hysteresis loops for BNBT-BSN-xCZFMO ceramics with various CZFMO content, measured under an electric field of 40 kV/cm at room temperature, are presented in Figure 8. A saturated and pinched loop was observed for the pure BNBT-BSN ceramic (x=0) with a high maximum polarization (P_{max} of 33.19 μC/cm^2), remnant polarization (P_r of 26.09 μC/cm^2), and coercive field (E_c of 14.22 kV/cm), consistent with relaxor ferroelectric behavior and the findings of A. Luangpangai *et al*. (Luangpangai *et al*., 2024). The P-E loop saturation decreased as CZFMO content increased. A small amount of CZFMO (x=0.05), led to slimmer P-E loops and a reduction in P_{max} (14.68 μC/cm^2), P_r (5.16 μC/cm^2), and E_c (11.06 kV/cm). As x increased to 0.10, the ceramic exhibited a broader P-E loop with P_{max} of 11.30 μC/cm^2, P_r of 11.73 μC/cm^2 and a large E_c of 24.99 kV/cm, suggesting significant leakage currents. This can be explained by decreased electrical resistance caused by the increased non-ferroelectric (ferrite) structure and the existence of secondary phases, as seen in the XRD analysis with increased CZFMO content. The added CZFMO lowered breakdown strength and voltage tolerance, resulting in a higher leakage current density (Gao *et al*. 2019).

At higher CZFMO levels (x>0.10), the P-E loops became narrower and P_{max}, P_r and E_c decreased (P_{max} of 5.45 μC/cm^2, P_r of 3.01 μC/cm^2 and E_c of 17.40 kV/cm for x=0.15 as well as P_{max} of 3.80 μC/cm^2, P_r of 2.09 μC/cm^2 and E_c of 17.39 kV/cm for x=0.20), as listed in Table 2. These results could be attributed to the introduction of charged defect acceptor ions, such as Fe^{3+} and Co^{2+}. These ions can form electric dipoles with oxygen vacancies, functioning as pinning points, limiting

dipolar rotation, and lowering coercivity. A similar effect was found in CZFMO-doped $PbZr_{0.52}Ti_{0.48}O_3$ ceramics, as reported by A. Gupta *et al*. (Gupta *et al*., 2011).

The magnetization-magnetic field (M-H) curves of BNBT-BSN-xCZFMO ceramics with different CZFMO content, measured over a field range of -15 to 15 kOe at room temperature, are shown in Figure 9(a-f). For the pure BNBT-BSN ceramic (x=0), the M-H curve had a negative slope with a remnant magnetization (M_r) of 9×10^{-5} emu/g, a saturation magnetization (M_s) of -0.0044 emu/g, and a coercive field (H_c) of 52 Oe (inset in Figure 9(a) and Table 2). The negative slope and small magnetization values suggest diamagnetic behavior. The slope became positive with a small amount of CZFMO content (x=0.05), indicating a transition to ferromagnetic behavior. The sample showed a higher M_r of 0.0009 emu/g, M_s of 0.0715 emu/g, and a lower H_c of 24 Oe, as seen in Figure 9(b) (inset) and Table 2. Ferromagnetic behavior develops due to structural distortion, which induces canting of the antiferromagnetic ordering chain (Futakuchi *et al*., 2014).

As CZFMO content increased to x=0.10-0.15, the M-H curves exhibited an increase in M_s (0.1411 emu/g for x=0.10 and 0.2485 emu/g for x=0.15), and a dramatic reduction in M_r (9×10^{-5} emu/g for x=0.10; 7×10^{-5} emu/g for x=0.15) and H_c (7 Oe for x=0.10; 3 Oe for x=0.15), as shown in the insets of Figure 9(c-d) and Table 2. As CZFMO increased to x=0.20, the M_s increased dramatically to 0.8056 emu/g with an H_c of 5 Oe (inset in Figure 9(e) and Table 2). The increase in M_s with higher CZFMO content is due to the CZFMO (ferrite) grains acting as centers of magnetization, with the overall saturation magnetization being the vector sum of these contributions (Mane *et al*., 2018). H_c is influence by magnetocrystalline anisotropy, microstrain, magnetic particle morphology, size distribution, shape anisotropy, and magnetic domain size (Priya *et al*., 2015). The higher M_s and lower H_c values at higher CZFMO levels indicate the ceramic's transition to more soft magnetic behavior. However, at higher doping levels, ferromagnetic behavior deteriorated with lower M_r and H_c, values, as seen in Figure 9(f) and its inset. This reduction was induced by excessive ion doping, consistent

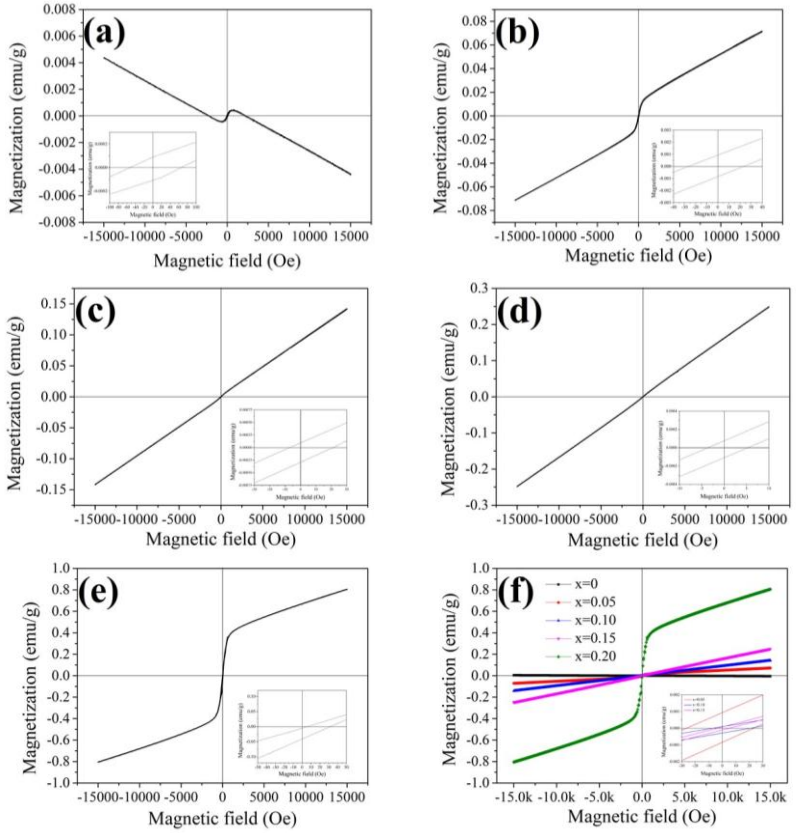

Figure 9. Magnetic behavior of BNBT-BSN-xCZFMO ceramics, indicating a transition from diamagnetic to ferromagnetic with CZFMO doping at (a) x = 0, (b) x = 0.05, (c) x = 0.10, (d) x = 0.15, (e) x = 0.20, and (f) all x levels

with findings reported by Y. Wan *et al*. (Wan *et al*., 2014).

The magnetoelectric coupling coefficient (α_E) quantifies the interaction between the magnetic and electric properties of multiferroic materials and is calculated using the equation (Vopson *et al*., 2017):

$$\alpha_E = \frac{V_{out}}{tH_{AC}} \quad (1)$$

The induced output voltage (V_{out}) was measured in a DC magnetic field with an applied AC magnetic field (H_{AC}) of 10 Oe and a frequency of 1.5 kHz, while t is the sample thickness. The α_E values for BNBT-BSN-xCZFMO ceramics with various CZFMO levels with a DC magnetic field (H_{dc}) ranging from 0 to 5000 Oe are shown in Figure 10. At H_{dc} of 1000 Oe, α_E values continually increased from 1.317 to 5.111 mV/Oe·cm when x increased from 0 to 0.20, as listed in Table 2. The result could be related to the higher magnetostriction produced by the higher mass ratio of CZFMO contents, consistent with a similar report by C. S. Chitra Lekha *et al*. (Chitra Lekha *et al*., 2019).

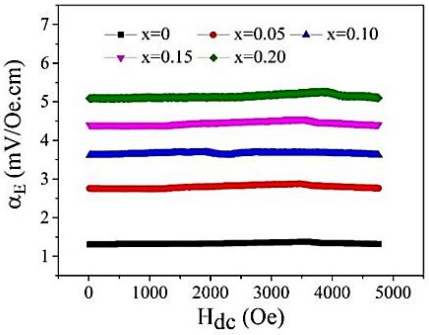

Figure 10. Variations in α_E and H_{dc} of BNBT-BSN-xCZFMO ceramics with different x levels

The 0.90BNBT-BSN-0.10CZFMO ceramic, fabricated using the solid-state combustion technique, exhibited optimal electrical, magnetic and magnetoelectric properties (ε_r of 674, P_{max} of 11.30 μC/cm^2, P_r of 11.73 μC/cm^2, M_s of 0.1411 emu/g, M_r of 9×10^{-4} emu/g, H_c of 7 Oe and α_E of 3.655 mV/Oe.cm). Other multiferroic ceramics, such as $0.90Bi_{0.465}Na_{0.465}Ba_{0.07}TiO_3$-$0.10Ni_{0.3}Cu_{0.08}Zn_{0.62}Fe_2O_4$, exhibited a P_{max} of ~1 μC/cm^2, P_r of ~0.7 μC/cm^2 and M_r of 7.55×10^{-6} emu/g (Nanda *et al*., 2019). Similarly, $0.90Ba_{0.9}Sr_{0.1}Zr_{0.04}Ti_{0.96}O_3$-$0.10Ni_{0.8}Zn_{0.2}Fe_2O_4$ multiferroic ceramics had a P_r of ~8 μC/cm^2 and α_E of 1.8 mV/Oe.cm (Rani *et al*., 2017), while $0.7BaTiO_3$-$0.3Ni_{0.7}Zn_{0.3}Fe_2O_4$ ceramics had an α_E of 0.124 mV/Oe.cm (Zhang *et al*., 2013). These comparisons highlight that 0.90BNBT-BSN-0.10CZFMO ceramics are a promising candidate for application in magnetoelectric devices and materials.

Conclusions

In summary, $(1-x)[0.99Bi_{0.47}Na_{0.47}Ba_{0.06}TiO_3$-$0.01Ba(Sn_{0.70}Nb_{0.24})O_3]$-$xCo_{0.6}Zn_{0.4}Fe_{1.7}Mn_{0.3}O_4$ multiferroic ceramics (abbreviated as BNBT-BSN-xCZFMO) with x=0-0.20 were successfully synthesized using the solid-state combustion technique. The phase structure, microstructure, electrical, magnetic, and magnetoelectric properties were studied. The coexistence of the perovskite and spinel phases was confirmed with CZFMO substitution, with a reduction in lattice parameters as CZFMO content increased. In addition, ferroelectric and ferrite grains were detected in the microstructure of BNBT-BSN ceramics when CZFMO was added. The porosity increased while the measured density decreased with higher CZFMO contents. The ε_r dropped with increasing CZFMO, caused by inferior microstructure and density, while ε_m was unmeasurable due to high electrical conductivity. Due to a high leakage current, the P-E loops became slimmer at x=0.05 but broadened significantly at x=0.10, with higher P_{max}, P_r, and E_c. Further additions of CZFMO content caused the P-E loops to become thinner and reduced the P_{max}, P_r, and E_c. The M-H curves showed a transition to ferromagnetic behavior with increasing CZFMO, as M_s increased while H_c decreased, implying enhanced soft magnetic behavior. The α_E values gradually increased from 1.317 to 5.111 mV/Oe•cm when x increased from 0 to 0.20. The study demonstrates improved magnetoelectric properties at optimal doping levels, suggesting potential applications in multiferroic devices.

Acknowledgement

The research was funded by Faculty of Science, Naresuan University. The authors would also like to thank Asst. Prof. Dr. Kyle V. Lopin for his help with improving the manuscript.

References

Badapanda, T., Sahoo, S., and Nayak, P. (2017). Dielectric, ferroelectric and piezoelectric study of BNT-BT solid solutions around the MPB region. Materials Science and Engineering, 178:012032. https://doi.org/10.1088/1757-899X/178/1/012032

Bongkarn, T., Chootin, S., Pinitsoontorn, S., and Maensiri, S. (2016). Excellent piezoelectric and ferroelectric properties of KNLNTS ceramics with Fe_2O_3 doping synthesized by

the solid state combustion technique. Journal of Alloys and Compounds, 682:14-21. https://doi.org/10.1016/j.jallcom.2016.04.285

Cao, W.P., Li, W.L., Dai, X.F., Zhang, T.D., Sheng, J., Hou, Y.F., and Fei, W.D. (2016). Large electrocaloric response and high energy-storage properties over a broad temperature range in lead-free NBT-ST ceramics. Journal of the European Ceramic Society, 36(3):593-600. https://doi.org/10.1016/j.jeurceramsoc.2015.10.019

Chandrasekhar, M., and Kumar, P. (2015). Synthesis and characterizations of BNT-BT and BNT-BT-KNN ceramics for actuator and energy storage applications. Ceramics International, 41(4):5574-5580. https://doi.org/10.1016/j.ceramint.2014.12.136

Chitra Lekha, C.S., Kumar, A.S., Vivek, S., Venkata Saravanan, K., Anantharaman, M.R., Surendran, K.P., Nandakumar, K., and Nair, S.S. (2019). Room temperature magnetoelectric properties of lead-free alkaline niobate based particulate composites. Ceramics International, 45(7):8115-8122. https://doi.org/10.1016/j.ceramint.2019.01.089

Futakuchi, T., Kakuda, T., and Sakai, Y. (2014). Multiferroic properties of $BiFeO_3$-$BaTiO_3$ based ceramics. Journal of the Ceramic Society of Japan, 122(1426):464-468. https://doi.org/10.2109/jcersj2.122.464

Gao, R., Qin, X., Zhang, Q., Xu, Z., Wang, Z., Fu, C., Chen, G., Deng, X., and Cai, W. (2019). Enhancement of magnetoelectric properties of (1-x) $Mn_{0.5}Zn_{0.5}Fe_2O_4$-$xBa_{0.85}Sr_{0.15}Ti_{0.9}Hf_{0.1}O_3$ composite ceramics. Journal of Alloys and Compounds, 795:501-512. https://doi.org/10.1016/j.jallcom.2019.05.013

Gupta, A., Huang, A., Shannigrahi, S., and Chatterjee, R. (2011). Improved magnetoelectric coupling in Mn and Zn doped $CoFe_2O_4$-$PbZr_{0.52}Ti_{0.48}O_3$ particulate composite. Applied Physics Letters, 98:112901.

Jia, Y., Fan, H., Wang, H., Yadav, A. K., Yan, B., Li, M., Quan, Q., Dong, G., Wang, W., and Li, Q. (2021). Large electrostrain and high energy-storage of (1-x)[0.94($Bi_{0.5}Na_{0.5}$)TiO_3-0.06$BaTiO_3$]-x$Ba(Sn_{0.70}Nb_{0.24})O_3$ lead-free ceramics. Ceramics International, 47(13):18487-18496. https://doi.org/10.1016/j.ceramint.2021.03.172

Jiang, J., and Ai, L.H. (2010). Synthesis and characterization of Fe-Co binary ferrospinel nanospheres via one-step nonaqueous solution pathway. Materials Letters, 64(8):945-947. https://doi.org/10.1016/j.matlet.2010.01.067

Kornphom, C., Saenkam, K., Jantaratana, P., Pinitsoontorn, S., and Bongkarn, T. (2023). Investigations on the multiferroic properties of lead free BNT-BCTS:MFO ceramic composites fabricated by the solid-state combustion technique. JOM, 75(7):2669-2683. https://doi.org/10.1007/s11837-023-05835-1

Lee, M.H., Kim, D.J., Park, J.S., Kim, S.W., Song, T.K., Kim, M.H., Kim, W.J., Do, D., and Jeong, I.K. (2015). High-performance lead-free piezoceramics with high Curie temperatures. Advanced Materials, 27(43):6976-6982. https://doi.org/10.1002/adma.201502424

Li, J.F., Wang, K., Zhu, F.Y., Cheng, L.Q., Yao, F.Z., and Green, D.J. (2013). (K,Na)NbO_3-based lead-free piezoceramics: Fundamental aspects, processing technologies, and remaining challenges. Journal of the American Ceramic Society, 96(12):3677-3696. https://doi.org/10.1111/jace.12715

Li, L., Hao, J., Xu, Z., Li, W., and Chu, R. (2016). 0.46% unipolar strain in lead-free BNT-BT system modified with Al and Sb. Materials Letters, 184:152-156. https://doi.org/10.1016/j.matlet.2016.07.150

Luangpangai, A., Jirattitikarn, T., Somsri, W., Rittidech, A., Prasertpalichat, S., and Bongkarn, T. (2024). Enhanced dielectric and ferroelectric properties near the morphotropic phase boundary in BNBT-BSN ceramics prepared by the solid-state combustion technique. Scientific Reports, 14(1):30268. https://doi.org/10.1038/s41598-024-81758-4

Mane, S.M., Tirmali, P.M., Ranjit, B., Khan, M., Khan, N., Tarale, A.N., and Kulkarni, S.B. (2018). Studies on magnetocapacitance, dielectric, ferroelectric, and magnetic properties of microwave sintered (1-x)($Ba_{0.8}Sr_{0.2}TiO_3$)-x($Co_{0.9}Ni_{0.1}Fe_2O_4$) multiferroic composite. Solid State Sciences, 81:43-50. https://doi.org/10.1016/j.solidstatesciences.2018.05.004

Nagata, H., Shinya, T., Hiruma, Y., Takenaka, T., Sakaguchi, I., and Haneda, H. (2006). Piezoelectric properties of bismuth sodium titanate ceramics. Ceramic Transactions, 167:213-221. https://doi.org/10.1002/9781118408186.ch20

Nanda, D., Kumar, P., Samanta, B., Sahu, R., and Singh, A. (2019). Structural, dielectric, ferroelectric and magnetic properties of (BNT-BT)-NCZF composites synthesized by a microwave-assisted solid-state reaction route. Journal of Electronic Materials, 48(8):5039-5047. https://doi.org/10.1007/s11664-019-07304-5

Parija, B., Badapanda, T., Rout, S.K., Cavalcante, L. S., Panigrahi, S., and Longo, E. (2013). Morphotropic phase boundary and electrical properties of 1-x[$Bi_{0.5}Na_{0.5}$]TiO_3-x$Ba[Zr_{0.25}Ti_{0.75}]O_3$ lead-free piezoelectric ceramics. Ceramics International, 39(5):4877-4886. https://doi.org/10.1016/j.ceramint.2012.11.080

Rani, R., Kumar, P., Singh, S., Juneja, J.K., and Prakash, C. (2017). Improvement in magnetoelectric and other physical properties of BSZT-NZF composites by microwave sintering. Journal of Alloys and Compounds, 690:716-719. https://doi.org/10.1016/j.jallcom.2016.08.119

Priya, A.S., Banu, I.B.S., and Chavali, M. (2015). Influence of (La, Cu) doping on the room temperature multiferroic properties of $BiFeO_3$ ceramics. Arabian Journal of Science and Engineering, 40(7):2079-2084. https://doi.org/10.1007/s13369-015-1668-z

Singh, H., Kumar, A., and Yadav, K.L. (2011). Structural, dielectric, magnetic, magnetodielectric and impedance spectroscopic studies of multiferroic $BiFeO_3$-$BaTiO_3$ ceramics. Materials Science and Engineering B, 176(7):540-547. https://doi.org/10.1016/j.mseb.2011.01.010

Singh, M., Singh, J., Kumar, M., and Kumar, S. (2020). Investigations on multiferroic properties of lead free (1-x)BCZT-xCZFMO based particulate ceramic composites. Solid State Sciences, 108:106380. https://doi.org/10.1016/j.solidstatesciences.2020.106380

Sinkruason, T., Luangpangai, A., Charoenthai, N., Rittidech, A., Pulphol, P., Vittayakorn, N., and Bongkarn, T. (2023). Phase formation and electrical properties of SBNLT ceramics prepared via combustion technique. Materials Science and Technology. 39(18):3065-3075. doi:10.1080/02670836.2023.2238415

Swain, S., Kar, S.K., and Kumar, P. (2015). Dielectric, optical, piezoelectric and ferroelectric studies of NBT-BT ceramics near MPB. Ceramics International, 41(9):10710-10717. https://doi.org/10.1016/j.ceramint.2015.05.005

Thatawong, B., Bhupaijit, P., Lamyai, Y., Vittayakorn, N., and Bongkarn, T. (2022). Dielectric and piezoelectric properties near the morphotropic phase boundary for 0.94BNT-0.06BT ceramics synthesized by the solid-state combustion technique. Ferroelectrics, 586(1):199-212. https://doi.org/10.1080/00150193.2021.2014271

Thawong, P., Punlek, N., Pinitsoontorn, S., and Bongkarn, T. (2019). Effect of the firing temperature on the phase formation, dielectric and ferromagnetic properties of CZFMO ceramics fabricated by the solid-state combustion technique. Ferroelectrics, 552(1):10-22. https://doi.org/10.1080/00150193.2019.1653078

Venkata Ramana, E., Graça, M.P.F., Monteiro, J., Mendiratta, S.K., and Valente, M.A. (2012). Improved magnetoelectric effect in modified $(Na_{0.5}Bi_{0.5})TiO_3$-$BaTiO_3$-$CoFe_2O_4$ lead-free multiferroic composites. In Proceedings of ISAF-ECAPD-PFM 2012 (pp. 1-4). https://doi.org/10.1109/ISAF.2012.6297834

Vopson, M.M., Fetisov, Y.K., Caruntu, G., and Srinivasan, G. (2017). Measurement techniques of the magneto-electric coupling in multiferroics. Materials, 10(8):963. https://doi.org/10.3390/ma10080963

Wan, Y., Li, Y., Li, Q., Zhou, W., Zheng, Q., Wu, X., Xu, C., Zhu, B., and Lin, D. (2014). Microstructure, ferroelectric, piezoelectric, and ferromagnetic properties of Sc-modified $BiFeO_3$-$BaTiO_3$ multiferroic ceramics with MnO_2 addition. Journal of the American Ceramic Society, 97(6):1809-1818. https://doi.org/10.1111/jace.12827

Wang, C., and Shi, P. (2023). $Bi_{0.2}Sr_{0.7}TiO_3$-doped $Bi_{0.5}Na_{0.5}TiO_3$-based lead-free ceramics with good energy storage properties. Journal of Materials Science: Materials in Electronics, 34:1774.

Wu, M.S., Tian, Z.M., Yuan, S.L., Duan, H.N., and Qiu, Y. (2012). Dielectric behavior and AC conductivity in Aurivillius $Bi_4Ti_3O_{12}$ doped by antiferromagnetic $BiFeO_3$. Physics Letters A, 376(28-29):2062-2066. https://doi.org/10.1016/j.physleta.2012.01.012

Xiao, S.H., Luo, K., and Zhang, L. (2010). The structural and magnetic properties of cobalt ferrite nanoparticles formed in situ in silica matrix. Materials Chemistry and Physics, 123(2-3):385-389. https://doi.org/10.1016/j.matchemphys.2010.04.026

Zawar, S., Atiq, S., Tabasum, M., Riaz, S., and Naseem, S. (2019). Highly stable dielectric frequency response of chemically synthesized Mn-substituted $ZnFe_2O_4$. Journal of the Saudi Chemical Society, 23(4):417-426. https://doi.org/10.1016/j.jscs.2018.06.010

Zhang, H., Zhou, J., Shen, J., Yang, X., Wu, C., Han, K., Zhao, Z., and Chen, W. (2017). Enhanced piezoelectric property and promoted depolarization temperature in Fe-doped $Bi_{1/2}(Na_{0.8}K_{0.2})_{1/2}TiO_3$ lead-free ceramics. Ceramics International, 43(18):16395-16402. https://doi.org/10.1016/j.ceramint.2017.09.015

Zhang, R.F., Deng, C.Y., Ren, L., Li, Z., and Zhou, J.P. (2013). Dielectric, ferromagnetic and magnetoelectric properties of $BaTiO_3$-$Ni_{0.7}Zn_{0.3}Fe_2O_4$ composite ceramics. Materials Research Bulletin, 48(10):4100-4104. https://doi.org/10.1016/j.materresbull.2013.06.026

Zou, M., Fan, H., Chen, L., and Yang, W. (2010). Microstructure and electrical properties of (1-x)[$0.82Bi_{0.5}Na_{0.5}TiO_3$-$0.18Bi_{0.5}K_{0.5}TiO_3$]-x$BiFeO_3$ lead-free piezoelectric ceramics. Journal of Alloys and Compounds, 495(1):280-283. https://doi.org/10.1016/j.jallcom.2010.02.025